DOI: 10.1002/chem.201501104



#### ■ Electrocatalysis

## Molecular Mixed-Metal Manganese Oxido Cubanes as Precursors to Heterogeneous Oxygen Evolution Catalysts

Sandy Suseno, [a] Charles C. L. McCrory, [b] Rosalie Tran, [c] Sheraz Gul, [c] Junko Yano, \*[c] and Theodor Agapie\*[a]

Abstract: Well-defined mixed-metal  $[CoMn_3O_4]$ [NiMn<sub>3</sub>O<sub>4</sub>] cubane complexes were synthesized and used as precursors for heterogeneous oxygen evolution reaction (OER) electrocatalysts. The discrete clusters were dropcasted onto glassy carbon (GC) and indium tin oxide (ITO) electrodes, and the OER activities of the resulting films were evaluated. The catalytic surfaces were analyzed by various techniques to gain insight into the structure-function relationships of the electrocatalysts' heterometallic composition. Depending on preparation conditions, the Co-Mn oxide was found to change metal composition during catalysis, while the Ni-Mn oxides maintained the NiMn<sub>3</sub> ratio. XAS studies provided structural insights indicating that the electrocatalysts are different from the molecular precursors, but that the original NiMn<sub>3</sub>O<sub>4</sub> cubane-like geometry was maintained in the absence of thermal treatment (**2-Ni**). In contrast, the thermally generated **3-Ni** develops an oxide-like extended structure. Both **2-Ni** and **3-Ni** undergo structural changes upon electrolysis, but they do not convert into the same material. The observed structural motifs in these heterogeneous electrocatalysts are reminiscent of the biological oxygenevolving complex in Photosystem II, including the MMn<sub>3</sub>O<sub>4</sub> cubane moiety. The reported studies demonstrate the use of discrete heterometallic oxide clusters as precursors for heterogeneous water oxidation catalysts of novel composition and the distinct behavior of two sets of mixed metal oxides.

#### Introduction

Metal oxides have been extensively studied as electrocatalysts for the oxidation of water in the oxygen evolution reaction [OER; Eq. (1)]. Typically, metal oxide films are obtained through precipitation, anodic electrodeposition, or adsorption/deposition onto the support materials (Fe, Co, Ni, Ir, Ru, Mn). [2]

$$2 H_2 O \rightarrow O_2 + 4 H^+ + 4 e^- \tag{1}$$

The detailed mechanism for the formation of the O–O bond is still under debate although several mechanistic pathways have been proposed. A general mechanism for the OER on metal oxides involves water coordination to the surface active site followed by a proton transfer to the solvent and an electron transfer to the electrode to form a surface M–OH species. Subsequently, a metal–oxo species is generated by proton-cou-

[a] S. Suseno, Prof. T. Agapie
 Division of Chemistry and Chemical Engineering
 California Institute of Technology, 1200 East California Boulevard
 MC 127-72, Pasadena, California 91125 (USA)
 E-mail: agapie@caltech.edu

[b] Dr. C. C. L. McCrory Joint Center for Artificial Photosynthesis Pasadena, California 91125 (USA)

[c] Dr. R. Tran, Dr. S. Gul, Dr. J. Yano Physical Biosciences Division, Lawrence Berkeley National Laboratory Berkeley, California 94720 (USA)

Supporting information for this article is available on the WWW under http://dx.doi.org/10.1002/chem.201501104.

pled oxidation or disproportionation of two M-OH species to lose H<sub>2</sub>O. Generation of O<sub>2</sub> is proposed to arise from reaction of two metal-oxo moieties or by attack of water or hydroxide on a metal-oxo moiety. Despite the lack of full mechanistic insight into this transformation, all proposals suggest the importance of the M-OH intermediates, and subsequently, the M-O bond in OER electrocatalytic activity. OER activity has been shown to linearly correlate to the standard enthalpy of formation of the corresponding M(OH)<sub>3</sub> for late first-row transition metal perovskites.<sup>[4]</sup> O<sub>2</sub> evolution has been proposed to follow metal oxide redox transitions as shown by a linear correlation between the minimum potential required for OER and the catalysts' lower oxide/higher oxide redox potentials.<sup>[5]</sup> A "volcano plot" relates the OER activity to the M-O bond strength by correlating the overpotential of certain metal oxides at a fixed current density to the enthalpy of a lower-to-higher oxide transition. [6] With these mechanistic proposals for homometallic oxides, mixed-metal oxides with weaker M-O bonds are expected to display enhanced OER behavior.

The OER activity of mixed metal oxides, especially in spinels, has been examined to determine the heterometallic effect relative to each homometallic oxide. The enhanced activity has been proposed to be correlated to the changes in the enthalpy of the metal oxide oxidation state transition and work function upon metal atom substitution. Some of the mixed metal oxides that have shown enhanced OER activity are Ni–Fe, Ni–Co, Ni–Co, Ni–Cu, Ni–Cu, Ni–Co–Fe, Ni–Co–Mo, Ni–Co–Mo, Ni–Cu, Ni–Cu, Mixed oxides of three or more metal combinations such as Co–Cr–Fe and Ni–Fe–M have also





been reported as OER electrocatalysts with enhanced activity.  $^{[9k,18]}$ 

The preparation of mixed metal oxide material with controlled metal-to-metal stoichiometry has been challenging as binary metal oxide films typically have bulk- and surface-metal compositions that differ from the stoichiometry of the precursor solutions. [9c, 16a, 19] Recently, a photochemical metal-organic deposition method has been reported as a facile technique for preparing amorphous phases of mixed metal oxides with controlled stoichiometry and high OER electrocatalytic activity. [20] Although many metal oxides have been reported for OER, composition–function relationships of heterometallic oxides have been less extensively studied, in part due to challenges in preparing controlled composition and structure. [7a, 9c, 16a, 21]

Molecular multimetallic complexes have been shown to serve as precursors to heterogeneous or supported OER catalysts. [2], 22] Employing well-defined heterometallic clusters as precursors is a potential strategy for maintaining metal stoichiometry and relative metal arrangement in the resulting heterogeneous OER catalysts. Herein, we employ discrete synthetic cluster precursors for the synthesis of bimetallic oxides active for electrolytic water oxidation. The effect of the preparation method and type of precursor on the composition, structure, and electrocatalytic performance of the heterogeneous oxide is evaluated. Maintaining the ratio of two metals during electrolysis is dependent on the nature of the components.

#### **Results and Discussion**

We recently developed a synthetic protocol for the synthesis of heterometallic manganese oxido cubane clusters [MMn<sub>3</sub>O<sub>4</sub>] that incorporate redox-active metals M (Scheme 1, 1-M;  $M = Fe^{3+}$ ,  $Co^{3+}$ ,  $Ni^{2+}$ ,  $Cu^{2+}$ ) by transmetalation of 1-Ca. These are structurally analogous to the previously investigated complexes (where  $M = Ca^{2+}$ ,  $Sr^{2+}$ ,  $Zn^{2+}$ ,  $Y^{3+}$ ,  $Sc^{3+}$ ,  $Mn^{3+}$ ).[23] These clusters serve as precursors to ternary metal oxides of controlled M/Mn ratio of 1:3. The catalytically active metal oxide films were prepared by dropcasting solutions of 1-M (M=Co, Ni) in dimethylformamide (DMF) onto the surface of indium tin oxide (ITO) on glass substrates or glassy carbon (GC) disk electrodes (Scheme 1). Removal of solvent under vacuum yielded a thick layer of film, 2-M that was treated to generate the catalyst (Scheme 1). Another method used to prepare a different material 3-M involves heating the dried film 2-M to remove the organic ligands (L and acetates) from the metal-oxido core (Scheme 1).

The electrochemical behavior of the materials **2-M** and **3-M** were studied in basic aqueous media and the steady-state current densities (j) were recorded as a function of the overpotential ( $\eta$ ) to probe the kinetics of the reaction. Upon electrolysis in basic media (pH 13 or 14) and release of gas, the top layer of the dropcasted film **2** was observed to fall into solution,

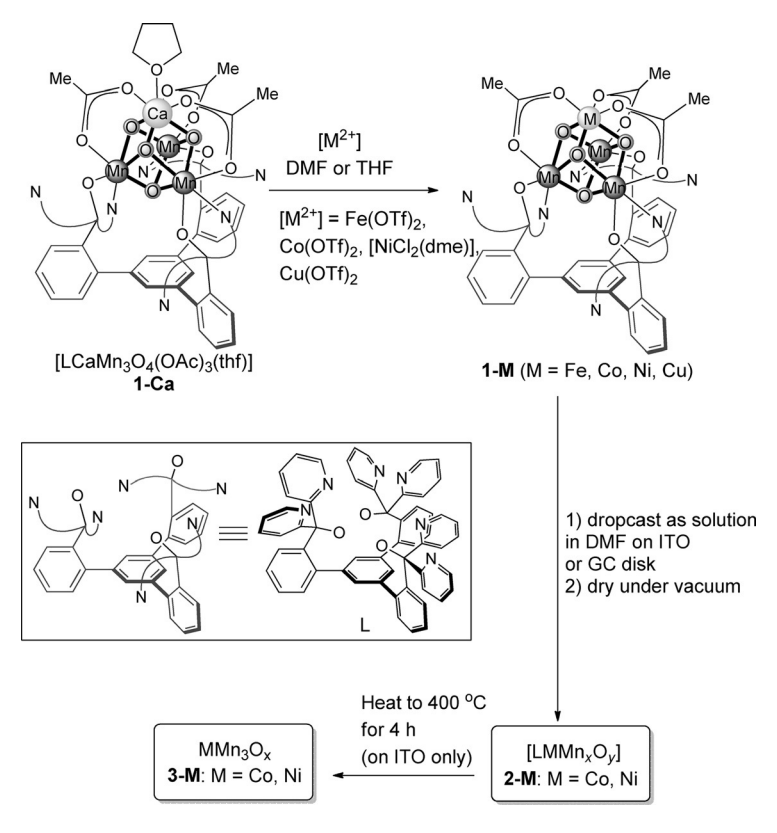
www.chemeurj.org

producing the catalytically active thin layer (< 200  $\mu m$ ) on the electrode.

Rotating disk voltammetry (RDV) measurements, chronopotentiometry (CP), and chronoamperometry (CA) studies, all at 1600 rpm, were performed to investigate the activity of the resulting surface material before and after 2 h electrolysis ( $t_{\rm CP}=0$  and 2 h; Figure 1 a–c) by evaluating the overpotential required to achieve current densities of 10 mA cm<sup>-2</sup> ( $\eta_{j=10\,{\rm mAcm^{-2}}}$ ) as the metric relevant for solar fuel synthesis.<sup>[7a]</sup> In addition, the current density of each catalyst on ITO was measured as a function of the overpotential (Tafel plot) in static solutions of 0.1 m KOH (Figure 2) from cyclic voltammetry (CV) measurements. The corresponding Tafel slopes,  $\eta_{j=10\,{\rm mAcm^{-2}}}$  values from RDV studies, and the overpotentials required to achieve current densities of 1 mA cm<sup>-2</sup> from static CV measurements are shown in Table 1.

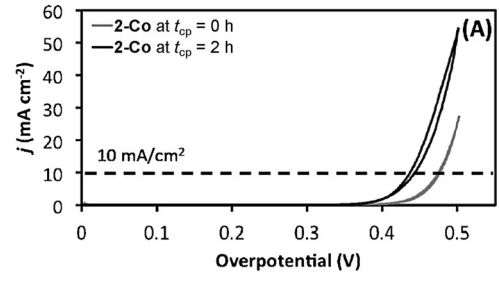
Table 1. Tafel slopes and overpotential parameters for 2 and 3.						
Catalyst	Tafel slope $[mV dec^{-1}]^{[a]}$	$\eta_{j=1\mathrm{mAcm^{-2}}}\mathrm{[V]^{[a]}}$	$\eta_{j=10~{\rm mAcm^{-2}}}~{ m [V]^{[b]}}$			
2-Co	42±5	$0.39 \pm 0.02$	$0.47 \pm 0.01$			
2-Co 3-Co	$69\pm 9$	$\textbf{0.45} \pm \textbf{0.2}$	-			
2-Ni	$40\pm 4$	$\textbf{0.37} \pm \textbf{0.01}$	$\textbf{0.42} \pm \textbf{0.01}$			
3-Ni	$58\pm1$	$0.38 \pm 0.01$	-			

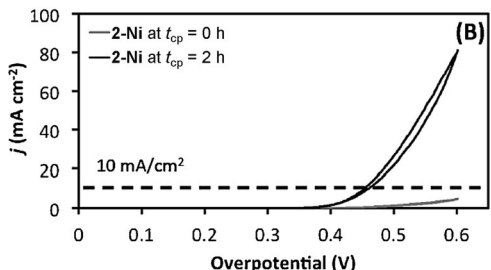
[a] Tafel slope and  $\eta_{j=1\,\mathrm{mAcm^{-2}}}$  parameters are derived from CP experiments on materials **2-M** and **3-M** dropcasted on ITO glass. Electrochemical experiments were performed in 0.1  $\,\mathrm{m}$  KOH. [b] **2-Co** and **2-Ni** were dropcasted on GC disk for various electrochemical experiments using RDV. [9]



Scheme 1. Synthetic route for the preparation of [LMMn $_x$ O $_y$ ] (2) and MMn $_3$ O $_x$  (3). Heating of 2 at 400 °C yields 3 through calcination of organic ligands.







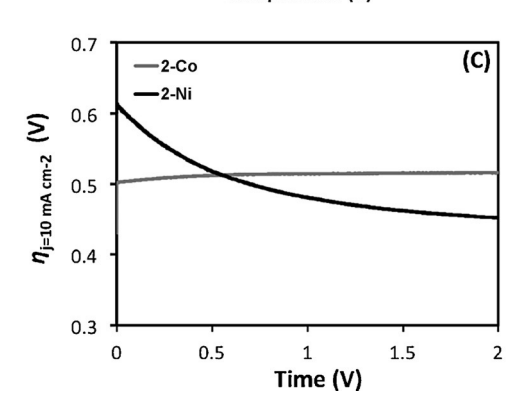


Figure 1. RDV of 2-Co (A) and 2-Ni (B) on glassy carbon disks before and after 2 h CP in 1  $\,\mathrm{M}$  NaOH solution; C) stability test of 2 over 2 h of CP held at 10  $\,\mathrm{mA\,cm^{-2}}$  at 1600 rpm rotation rate.

The elemental compositions of **2-M** and **3-M** were determined by X-ray photoelectron spectroscopy (XPS), energy dispersive X-ray spectroscopy (EDS), and inductively coupled plasma mass spectrometry (ICP-MS). The results from the three techniques are summarized in Table 2.

Prior to electrolysis, the dropcasted films **2-Co** and **2-Ni** showed M/Mn ratios of approximately 1:3 based on XPS and EDS (only XPS data are shown in Table 1 for this series) consistent with ratio in the molecular precursors **1-Co** and **1-Ni**. The elemental composition analyses of the resulting metal oxide

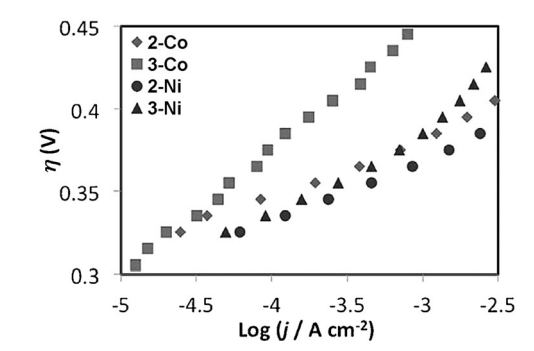


Figure 2. Tafel plots of the metal oxides on ITO: 2-Co (diamonds), 3-Co (squares), 2-Ni (circles), and 3-Ni (triangles).

films *after* electrolysis (1–5 h of CP) showed retention of the approximately 1:3 M/Mn ratio for **2-Ni**, **3-Co**, and **3-Ni**, but resulted in a lower average Co/Mn ratio of 1:1.2 for **2-Co** (Table 2). Neither the **2-Co** and **2-Ni** films after electrolysis nor the **3-Co** and **3-Ni** films gave rise to N 1 s peaks by XPS, indicating the loss of ligand L upon electrolysis or heat treatment, respectively. This is supported by the thermogravimetric analysis of **1-Co** (see the Supporting Information, Figure S1) where the loss of roughly 77% mass was observed upon heating at 400 °C for 4 h, consistent with calculated mass loss of all ligands (acetates and L) at around 78%. ICP-MS studies were carried out only on the resulting materials after electrolysis of **2-M** on the GC disks to avoid signal saturation by ITO.

Scanning electron microscopy (SEM) was used to characterize the surface morphologies for all metal oxide films 2 and 3 (Figure 3). The initial surface of the dropcasted material (in this case 1-Co) is shown in Figure 3a as a thick amorphous layer on the ITO electrode. Following water electrolysis (CP at 5 mA cm<sup>-2</sup>) with this material for 5 h, the resulting material consisted of a very thin electroactive metal oxide layer (Figure 3c). Figures 3b and 3d show the resulting thermally treated electroactive layer of 3-Co and 3-Ni respectively before and after electrolysis, where no obvious change on the surface morphology was observed. Figures 3e and 3f display the crystalline-looking final thin-layer film of 2-Ni after electrolysis from the top view and the cross-section, respectively. In addition to SEM, elemental mapping of the surfaces was also performed. The elemental maps of 3-Ni and 2-Co on ITO electrode are displayed in Figure 4. The elemental map reveals the uniformly scattered presence of Ni and Mn in the heterogene-

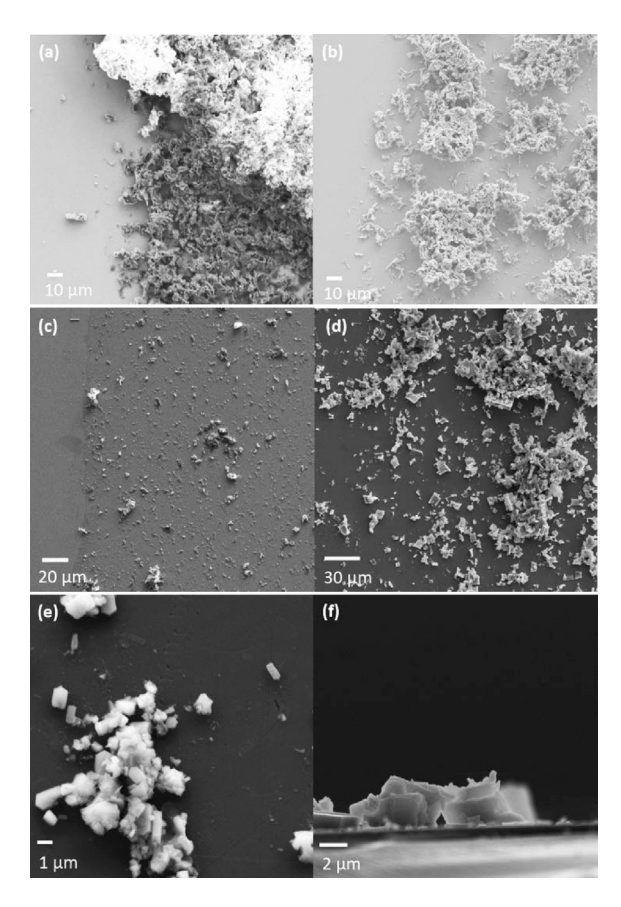
ous material. This observation is in contrast to the Co-containing materials, in which Co was detected throughout the surface whereas Mn was more localized on the "island" (Figure 4). Powder X-ray diffraction studies of these surfaces showed no patterns other than those resulting from the background ITO electrode (see the Supporting Information, Figure S5), indicating

Table 2. Normalized relative metal stoichiometry of catalyst films by XPS, EDS, and ICP-MS.												
	XPS				EDS				ICP-MS <sup>[a]</sup>			
	Bei	fore el	ectrolysis	Af	ter ele	ectrolysis	After electrolysis					
Catalyst	Co	Ni	Mn	Со	Ni	Mn	Со	Ni	Mn	Со	Ni	Mn
2-Co	1	-	$3.4 \pm 0.2$	1	-	$1.2 \pm 0.3$	1	-	$1.3\pm0.7$	1	-	$1.1\pm0.2$
3-Co	1	-	$3.9\pm0.4$	1	-	$3.9\pm1.0$	1	-	$\textbf{3.1} \pm \textbf{0.4}$	n/a		
2-Ni	-	1	$2.8\pm0.1$	-	1	$3.4\pm0.3$	-	1	$2.9 \pm 0.8$	-	1	$2.1\pm0.3$
3-Ni	-	1	$3.4 \pm 0.2$	-	1	$3.6\pm1.1$	-	1	$2.8\pm0.3$	n/a		

[a] ICP-MS analyses were only performed on **2-Co** and **2-Ni** after electrolysis on GC disks to prevent signal saturation from ITO.

www.chemeurj.org





**Figure 3.** SEM images of ITO electrode surfaces with: a) **1-Co** initially drop-casted pre-electrolysis; b) **3-Co** pre- and post-electrolysis; c) **2-Co** post-electrolysis; d) **3-Ni** pre- and post-electrolysis; e) **2-Ni** post-electrolysis; f) cross section side-view of electrode with **2-Ni** post-electrolysis.

that they are either amorphous or possibly too thin for detection (ca. 2  $\mu$ m thickness; Figure 3 f).

RDV and CP studies of **2-Co** show similar activity at  $t_{\text{CP}} = 0$  h vs. 2 h (Figure 1 a, c). In contrast, the electrochemical studies on **2-Ni** film indicated that the initial film has low electrocatalytic activity for OER, but possibly structurally rearranges upon electrolysis to generate a more active material with improved overpotential to give 10 mA cm<sup>-2</sup> current density (Figure 1 b, c). The **3-Co** and **3-Ni** films retain similar electrocatalytic activity throughout the electrolysis period (see the Supporting Information, Figures S2 and S3). The observed overpotentials (0.36–0.43 V) to reach 1 mA cm<sup>-2</sup> current density for **2** and **3** (Figure 2, Table 1) as a measure of electrocatalytic activity are comparable to a number of other homo- and heterometallic oxide electrocatalysts. [Za-C,f,9h,i]

In addition, RDV studies of **2-Co** and **2-Ni** on GC electrodes resulted in  $\eta_{j=10\,\mathrm{mAcm^{-2}}}$  values and electrochemically active surface areas (ECSAs) that are comparable to other selected reported metal oxide films under identical conditions (Table 3). This suggests that both activity per geometric area and the specific activity per ECSA of **2-Co** and **2-Ni** are similar to other catalytic materials electrodeposited from metal salts. The amount of  $O_2$  produced by **2-Co** and **2-Ni** throughout 2 h constant current electrolyses at 1 mA cm<sup>-2</sup> was quantified using a fluorescent oxygen sensor and suggests nearly 100% Farada-

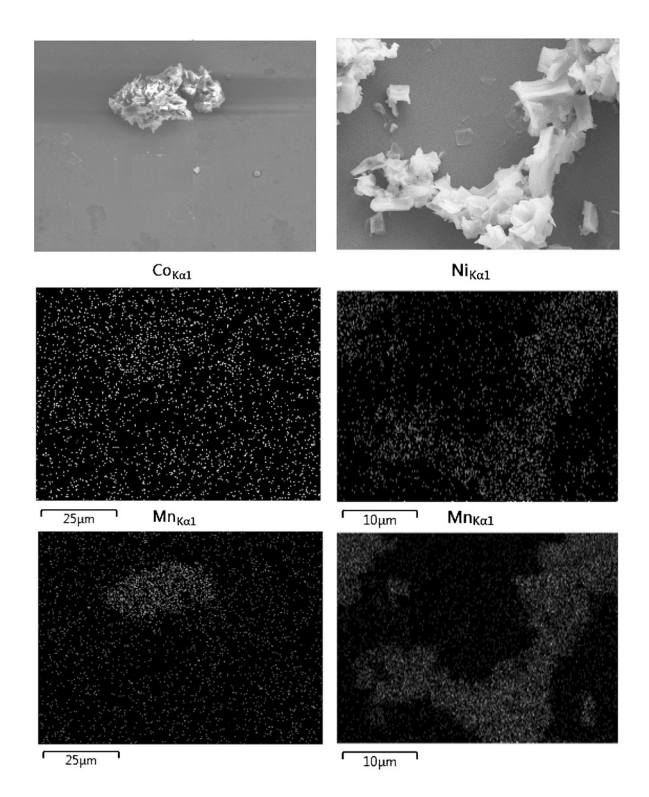


**Figure 4.** SEM images and elemental mappings of **2-Co** (left) and **3-Ni** (right) on ITO after electrolysis, displaying the SEM image with the corresponding Mn and Co/Ni $_{K\alpha 1}$  compositional maps.

 $\textbf{Table 3.} \ \, \textbf{Comparison of 2-Co} \ \, \textbf{and 2-Ni} \ \, \textbf{to selected metal oxide OER electrocatalysts}.$ 

Catalyst	ECSA [cm <sup>2</sup> ]	$\eta_{t=2h} \ [V^{-1}]$	ε
2-Co	2.0 ± 0.5	$0.47 \pm 0.01$	$0.97 \pm 0.04$
2-Ni	$1.8 \pm 0.5$	$0.42 \pm 0.01$	$1.00 \pm 0.05$
Co-(b) <sup>[a]</sup>	$1.9\pm0.6$	$0.40 \pm 0.04$	$0.97\pm0.01$
Co/P-(a) <sup>[a]</sup> ("CoP <sub>i</sub> ")	$\textbf{3.3} \pm \textbf{1.8}$	$0.38 \pm 0.02$	$\textbf{0.91} \pm \textbf{0.05}$
Ru-(a) <sup>[a]</sup>	$14\pm4$	$0.32 \pm 0.02$	$\boldsymbol{0.93\pm0.07}$
Ni-(b) <sup>[a]</sup>	$\textbf{0.4} \pm \textbf{0.2}$	$\textbf{0.47} \pm \textbf{0.03}$	$\boldsymbol{0.90\pm0.02}$
NiCo-(c) <sup>[a]</sup>	$1.8\pm0.8$	$0.35\pm0.01$	$\textbf{0.92} \pm \textbf{0.02}$
NiFe-(b) <sup>[a]</sup>	$0.8\pm0.2$	$\textbf{0.37} \pm \textbf{0.02}$	$\boldsymbol{0.93\pm0.02}$
NiMoFe-(b) <sup>[a]</sup>	$1.8\pm0.6$	$\textbf{0.33} \pm \textbf{0.02}$	$\boldsymbol{0.97 \pm 0.05}$
GC background <sup>[b]</sup>	$1.9\pm0.9$	$1.29 \pm 0.02$	$0.76\pm0.07$

ECSA = electrochemically active surface area ( $C_{DoubleLayer}/C_{Specific}$ );  $\eta_{t=2h}=$  overpotential at t=2 h,  $\varepsilon=$  faradaic efficiency. [a] see ref. [9k]; [b] see ref. [9i].

ic efficiency for the electrocatalytic process. These results indicate that the synthetic cubane complexes 1-M (M=Co, Ni) can serve as precursors to generate competent and selective OER electrocatalysts with applied oxidative potentials.

Further investigations of the final metal compositions of these electrocatalysts were performed to complement the results from the electrochemical studies. Material **2-Co** was observed to undergo the largest variation in M/Mn stoichiometry before vs. after 1–5 h electrolysis (Table 2). The reported value in Table 2 is an average of all analyzed spots on the non-uniform electrode surface, but there were multiple areas on the





electrode evaluated by XPS and EDS that displayed Co/Mn ratios of approximately 1:0.1; the Co  $2p_{3/2}$  peak was primarily the only metal signal observed in the spectrum. This result suggests that most of the Mn centers dissolved in the solution during electrocatalytic oxidation of hydroxide ions to  $O_2$ , likely as reduced metal species (Mn<sup>II</sup> and Mn<sup>III</sup>) that are soluble in water and kinetically labile. The generated catalyst, predominantly the homometallic cobalt oxide (CoO<sub>x</sub>) film, remains active for water oxidation.

The elemental analysis data for 2-Ni, 3-Co, and 3-Ni display retention of the metal stoichiometry even after prolonged electrolysis periods, providing evidence that the cluster cores may have stayed intact in those films, or that they have converted into materials that maintain the 3:1 Mn/M ratio. Additionally, elemental mapping of the surfaces of 2-Ni, 3-Co, and **3-Ni** (Figure 4 and Figure S17 in the Supporting Information) after electrolysis show no obvious phase separation of M and Mn, suggesting the retention and co-localization of both metals in the electrocatalysts. However, the elemental map of 2-Co after electrolysis shows variable distribution of Co and Mn on the larger island in comparison to the rest of the surface (Figure 4), consistent with the non-uniform electrodeposition of Co back onto the electrode throughout electrolysis. Further studies are required to determine whether structural rearrangements may have occurred or the electrodeposition of the dissociated M<sup>II</sup> salts back onto the electrode favors similar

1:3 M/Mn metal stoichiometry. Based on the elemental composition studies, 1-Co and 1-Ni can indeed serve as precursors to catalytically active materials for OER with control over M/Mn ratio for 2-Ni, 3-Co, and 3-Ni. demonstration suggests that the structure and composition of mixed-metal catalysts can be tuned by the selection of heterometallic molecular precursors. The variation in composition of 2-Co highlights the importance of thoroughly evaluating the compositions of metal oxide materials both before and after catalysis, especially for those heterometallic oxides that were not prepared by electrodeposition.

The Ni–Mn OER catalysts maintain the metal ratio despite being prepared under different conditions. However, the variation in catalytic properties of 2-Ni suggests that structural changes may occur during catalysis. X-ray absorption spectroscopic (XAS) studies were performed to determine whether the metal oxides underwent

structural changes/rearrangements during electrocatalysis. Figures 5 and 6 show the Mn and Ni XANES (X-ray absorption near-edge structure) and EXAFS (extended X-ray absorption fine structure) spectra of **2-Ni** at  $t_{\rm CP}\!=\!1$  and 5 h and **3-Ni** at  $t_{\rm CP}\!=\!0$ , 1, and 5 h, together with those of the dropcasted complex **1-Ni**. The EXAFS curve-fitting results of the selected samples are shown in the Supporting Information (Figure S18).

Both Mn and Ni data suggest that the Mn and Ni local environments of the dropcasted 1-Ni were altered during the electrolysis (2-Ni; Figures 5a,b and 6a,b) and more significantly by the heat treatment (3-Ni; Figures 5 c, d and 6 c, d). Although the Mn and Ni XANES edge positions of 2-Ni are close to those for 1-Ni and the EXAFS peak positions are essentially the same as those of 1-Ni, a significant reduction of the EXAFS peak intensity is observed (Figure 6 a, b). This indicates the wider range of metal-ligand and metal-metal distances in comparison to the original 1-Ni structure, and its effect is reflected in the larger Debye–Waller factors ( $\sigma^2$ ) of the metal–metal interactions in the EXAFS fit parameters of both Mn and Ni in 2-Ni (see the Supporting Information, Tables S1 and S2). There are no detectable peaks above the noise level in the long range (apparent distances in the range of 4-6 Å, Figure 6a,b) of 2-Ni, suggesting no formation of the extended oxide-like structure at this stage. This indicates the retention of the basic cubane core structure during electrolysis.

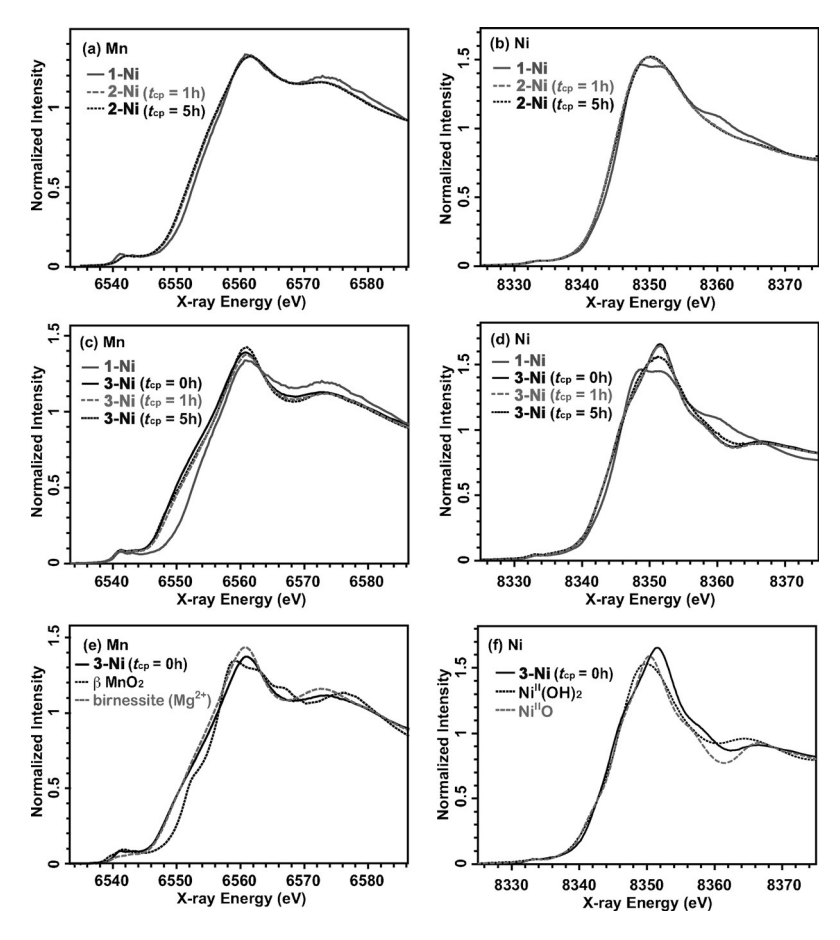


**Figure 5.** Mn (left) and Ni (right) XANES spectra of **1-Ni** with **2-Ni** at  $t_{CP} = 1$  and 5 h (a, b), and **3-Ni** at  $t_{CP} = 0$ , 1, 5 h (c, d). The spectra of **3-Ni** at  $t_{CP} = 0$  h are also compared with those of Mn and Ni oxides (e, f).



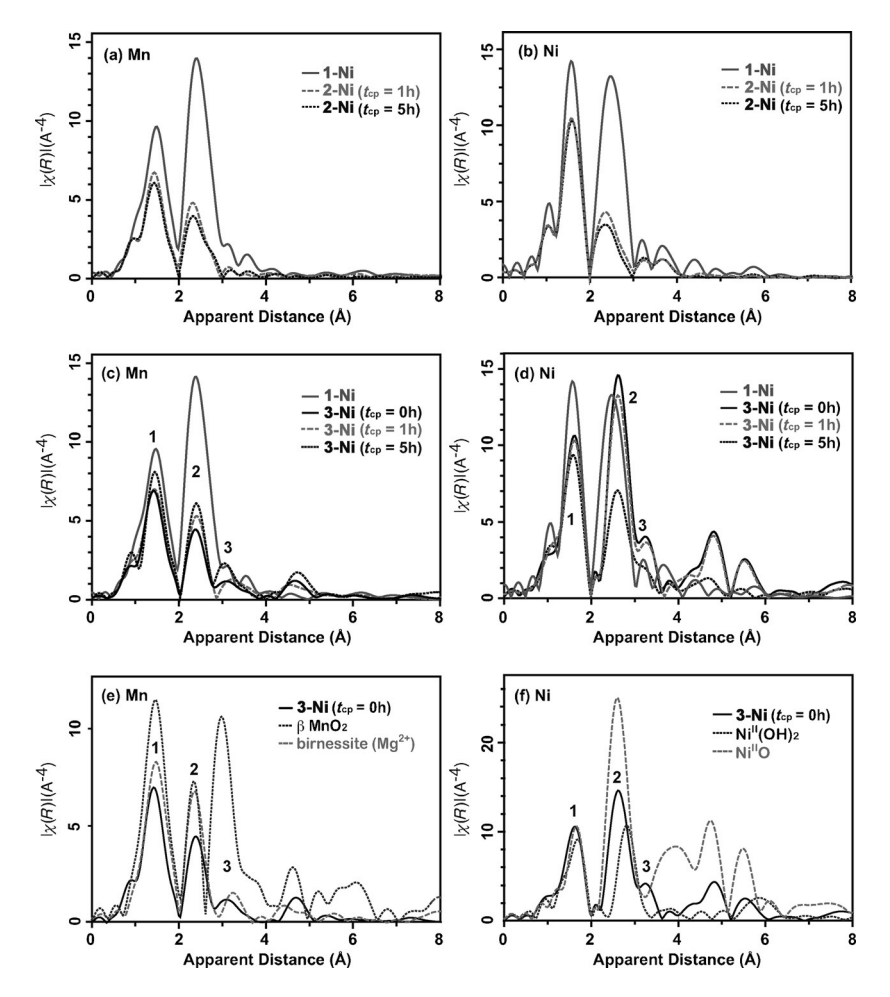


**Figure 6.** Mn (left) and Ni (right) EXAFS spectra of **1-Ni** with **2-Ni** at  $t_{CP} = 1$  and 5 h (a, b), and **3-Ni** at  $t_{CP} = 0$ , 1, 5 h (c, d). The spectra of **3-Ni** at  $t_{CP} = 0$  h are also compared with those of Mn and Ni oxides (e, f).

When the dropcasted 1-Ni is heat-treated (3-Ni), the Mn XANES rising edge positions are shifted to lower energy, suggesting the reduction of Mn from Mn<sup>IV</sup> (Figure 5c). A rise of the Mn and Ni EXAFS long range peaks (apparent distances in the range of 4-6 Å in Figure 6 c, d) in 3-Ni, that were not observed in 1-Ni or 2-Ni, are indicative of the formation of the extended structure like oxides and arises from multiple scattering paths. The Mn XANES and EXAFS spectra of the 3-Ni film at  $t_{\rm CP} = 0$  h mostly resembles the spectra of birnessites (Mn<sup>III/IV</sup> oxide) as shown in Figures 5 e and 6 e (Mg<sup>2+</sup> birnessite). This implies that in the **3-Ni** film (at  $t_{CP} = 0$  h) some fraction of Mn is reduced from the native Mn<sup>IV</sup> oxidation state in **1-Ni** to Mn<sup>III</sup>. A resemblance of the Mn XANES edge position to that of Mg<sup>2+</sup> birnessite, which has an oxidation state of approximately 3.7, suggests that roughly 30% of Mn is reduced to Mn<sup>III</sup> and the rest remains as  $Mn^{IV}$  in the **3-Ni** film (at  $t_{CP} = 0$  h). In contrast, the Ni remains as Ni<sup>II</sup> based on the Ni XANES edge position

Regarding the structure of **3-Ni**, Mn likely forms a layered structure that is similar to the birnessites, based on the similarities observed in both XANES and EXAFS (Figures 5e and 6e). Such structure has been observed in Mn oxide electrocatalysts that catalyze the oxygen evolution reaction, and a birnessite-

like phase seems to be dominant when Mn is electrochemically deposited on substrates. [2d, 16a, 21b, 24] However, the Ni EXAFS spectrum of 3-Ni is similar to that of Ni<sup>II</sup>(OH)<sub>2</sub>, which has a complete cubane structure. Although the peak positions of the metal-ligand (peak 1 in Figure 6e,f) and metal-metal interactions (peak 2 in Figure 6 e, f) are similar to the oxides (birnessite for Mn and Ni<sup>II</sup>O for Ni) in both Mn and Ni EXAFS, the intensity of the peak 2 in both cases is weaker, suggesting that the metal cluster is more disordered or it has small domain sizes compared to those of bulk oxides.

A question arises whether Ni is still incorporated into the Mn birnessite-like structure in **3-Ni**. As the XPS analysis shows retention of the Mn/Ni ratio of 3:1 in **3-Ni**, the fraction of Ni should be located either (1) systematically with Mn within the Mn layered structure, (2) randomly within the Mn layer, (3) between the Mn layers as 2<sup>+</sup> counter ions, or (4) as Ni oxide domains that are phase-separated from Mn domains.

The Mn and Ni EXAFS curve fitting of **3-Ni** ( $t_{CP} = 0$  h) was carried out to investigate the above four possibilities (see the Supporting Information, Figure S18). The Mn EXAFS curve fitting result shows a predominant Mn-metal distance of around 2.93 Å (peak 2 region in Figure 6 c, e; see also Table S1, 3-Ni fit 1, in the Supporting Information), whereas the Ni EXAFS shows a predominant Ni<sup>II</sup>-metal interaction at around 2.98 Å (peak 2 region in Figure 6 d,f; see also Table S2, 3-Ni fit 1, in the Supporting Information). This Ni<sup>II</sup>-metal distance is longer than the Ni<sup>II</sup>-Mn<sup>IV</sup> distances (2.83 Å) in the original **1-Ni** compound, and very similar to the Ni<sup>II</sup>-Ni<sup>II</sup> di-μ-oxo-bridged interactions (2.95 Å), typically observed in Ni<sup>II</sup>O oxide. Although this distance could also correspond to the Ni<sup>II</sup>-Mn<sup>III</sup> interactions, an overall resemblance of the 3-Ni Ni EXAFS peak positions to those of the Ni<sup>II</sup>O oxide spectrum indicates that the Ni domains in 3-Ni form Ni<sup>II</sup>O oxide-like Ni-Ni interactions (see the Supporting Information, Figure S19 for the k-space EXAFS data).

Based on the above observations, one hypothesis is that Mn and Ni form separate domains, Mn<sup>III/IV</sup> with a birnessite-like layered structure, and Ni with Ni<sup>II</sup>O oxide-like interactions (case (4) described above). However, the fit quality of the 3<sup>rd</sup> peak region in both Mn and Ni EXAFS of **3-Ni** was not sufficient (see



Figure S18 for 3-Ni), in spite of the fact that 1st and 2nd EXAFS peaks of both Mn and Ni EXAFS fit well with the structural parameters obtained from birnessite and Ni<sup>II</sup>O structures, respectively. A further comparison to a series of Mn oxides suggests that the peak 3 region in the Mn EXAFS of 3-Ni could reflect a presence of rutile-like metal-metal interactions with some oxygen with a trigonal planar coordination, that are observed in β-MnO<sub>2</sub> structure. To check whether these Mn–Ni interactions are present in 3-Ni for both Mn and Ni EXAFS, an additional Mn-Ni interaction was included in the fit (see the Supporting Information, Figure S18e and Tables S1 and S2, fit 2 for 3-Ni). The fit quality improved noticeably in the Ni EXAFS and marginally in the Mn EXAFS going from fit 1 to fit 2 in Table S1 and S2. Both Mn and Ni EXAFS suggest this metal-metal distance to be around 3.50-3.55 Å. Therefore, it is very likely that Mn and Ni are in a close proximity at around 3.5 Å in 3-Ni. Based on the above observations, together with the XPS and EDS results (Table 2) that show the Mn/Ni ratio to be close to 3:1 in **3-Ni**, a possible structural motif was built (Figure 7).

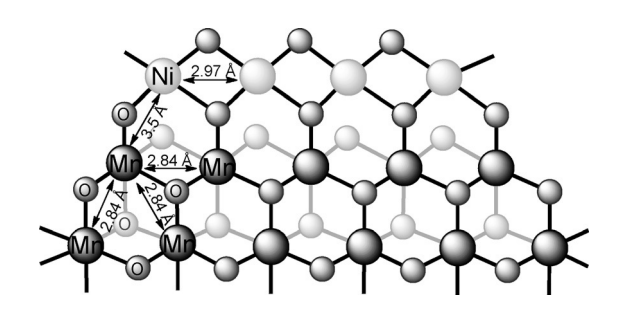


**Figure 7.** Structural model of **3-Ni**. Bridging oxo/hydroxo ligands, Mn centers, and Ni centers are displayed in different shades of gray. Estimated metal–metal and metal–ligand distances based on the EXAFS data are shown.

In the **3-Ni** film, both Mn and Ni are sensitive to electrolysis progression, as shown by the Mn and Ni XAS spectral changes for  $t_{\rm CP}\!=\!0$ , 1, and 5 h (Figures 5 c,d and 6 c,d). A reduction of the EXAFS peak intensity with no significant changes in the XANES edge position suggests that the Mn and Ni oxide domains become highly disordered during the electrolysis.

Although the identity of the active site for hydroxide oxidation to O2 is not known, the catalytic and spectroscopic studies reported here for NiMn<sub>3</sub> materials allow for some structurefunction speculations. The method of catalyst generation leads to different behaviors. Both 2-Ni and 3-Ni show structural changes compared to 1-Ni based on EXAFS. The material prepared without thermal treatment, 2-Ni, shows EXAFS features consistent with the maintenance of the NiMn<sub>3</sub>O<sub>4</sub> moiety, albeit with a wider range of metal-metal and metal-ligand distances. The EXAFS data indicate that the major structural change occurs within the first hour of electrolysis, and that there are no significant changes between  $t_{CP} = 1$  and 5 h. This correlates with RDV data (Figure 1 c) that show a gradual lowering in overpotential, with a larger effect at early times when the material is undergoing structural changes. The material prepared by thermal treatment, 3-Ni, has an extended oxide-like structure and is more structurally distinct from 1-Ni. Catalytic behavior is improved for 2-Ni. Both 2-Ni and 3-Ni show structural changes upon electrolysis, but they do not convert into the same material. This behavior indicates that the structural motif found in the homogeneous precursor may be roughly maintained in the heterogeneous mixed metal electrolysis catalyst, especially if high temperature treatment is avoided. The catalytic performance is affected by these structural differences.

#### Conclusion

Well-defined, synthetic 1-M cubane complexes were dropcasted on ITO or glassy carbon disk electrodes and used as precursors, with a known 1:3 M/Mn ratio, for OER electrocatalysts. Upon heat treatment at 400 °C and/or electrolysis, the OER activities of 2-M and 3-M were evaluated to be similar to many other reported homo- and heterometallic oxide electrocatalysts. 2-Ni requires structural rearrangement to yield the active species. The 2-Co film underwent compositional changes to give a CoO<sub>x</sub>-like material upon prolonged electrolysis, losing the majority of Mn into solution. The 2-Ni film may have rearranged structurally yet still retained its Ni/Mn ratio of 1:3 in the final material. The distinct behaviors of the heterogeneous OER electrocatalysts described here indicate that the composition and structural changes in post-electrolysis of heterometallic catalysts is critical in understanding the behavior of these catalysts. XAS studies provided structural insights of the electrocatalysts, establishing that the resulting 2-Ni film after electrolysis is indeed different from the initial 1-Ni synthetic precursor, while likely maintaining the original Mn<sub>3</sub>NiO<sub>4</sub> cubane-like geometry. In contrast, the thermally generated 3-Ni develops an oxide-like extended structure, with Mn oxide birnessites with μ-oxo-bridged Ni<sup>II</sup>–Ni<sup>II</sup> and mono-μ-oxo-bridged metal–metal (Mn<sup>|||/|V</sup>-Ni<sup>||</sup>) interactions. This is reminiscent of Ca-Mn oxides that display structural motifs related to the biological oxygen evolving complex in Photosystem II. [2k, 25] The above structural relations suggest a catalytic function of the MMn<sub>3</sub>O<sub>4</sub> cubane moiety. The use of molecular multimetallic oxido cubane precursors displaying two types of metals has been demonstrated as a facile method to access OER electrocatalysts of novel compositions and structures that allows for systematic study of changes in structure from discrete precursors to heterogeneous catalysts to post-catalysis materials.

#### **Experimental Section**

Materials synthesis and film preparation

#### **General considerations**

Unless otherwise specified, all compounds were manipulated under air. Dichloromethane (DCM) and DMF were purchased from J. T. Baker and EMD Millipore respectively. High-purity sodium hydroxide and potassium hydroxide were purchased from Sigma Aldrich. All water used was Milli-Q water purified by a Millipore water purification system (18.2 M $\Omega$  cm resistivity). ITO-coated glass slides (with surface resistivity 8–12  $\Omega$ /sq) were purchased from Sigma Aldrich. The complex **1-Ca** was synthesized according to lit-





erature procedure.<sup>[23a]</sup> Complexes **1-Co** and **1-Ni** are synthesized analogously to other reported **1-M**.<sup>[23b]</sup> The detailed synthesis and characterization of **1-Co** and **1-Ni** will be reported separately.

#### Preparation of 2-Co and 2-Ni

In a scintillation vial, **1-Co** or **1-Ni** (3 mg) was fully dissolved in DCM (0.3 mL). DMF (0.3 mL) was added into the solution, and the DCM solvent was allowed to evaporate in air. The DMF solution of **1-Co/Ni** was dropcasted using a Hamilton syringe onto 5 separate cleaned ITO-coated glass substrates (with a 0.5 cm $\times$ 0.5 cm window or geometric surface area of 0.25 cm $^2$ ) or glassy carbon (GC) disks equally in 60  $\mu$ L portions. The dropcasted solution on the electrodes was then dried under vacuum over 1 h to yield a thick film on the ITO. These resulting films, **2-Co** and **2-Ni**, were used as precursors to the catalytically active species after electrolysic

#### Preparation of 3-Co and 3-Ni

The dried films, **2-Co** and **2-Ni**, on ITO-coated glass substrate were then heated at  $400\,^{\circ}\text{C}$  in the thermolyne muffle furnace for  $\geq 4\,\text{h}$  to remove organic ligands and generate a non-uniform, thin metal oxide film on the ITO. Removal of organic ligands from **1-Co** was confirmed by thermogravimetric analysis (TGA; see the Supporting Information, Figure S1), and the analogous event is assumed to occur for **1-Ni**. These resulting films, **3-Co** and **3-Ni**, were used for further electrochemical experiments without further modification.

**Note**: preparation of **3-Co/Ni** on the GC disks was not conducted due to the possibility of compromising the GC electrode quality under high heat (400 °C) for prolonged periods of time.

#### Electrochemistry

Electrochemical measurements of **1-Co** and **1-Ni** were conducted with a Solarton 1287/1260 potentiostat/galvanostat with a built-in electrochemical impedance spectroscopy (EIS) analyzer. The working electrode was ITO on glass substrate, and catalysts were deposited as described above. The auxiliary electrode was a Pt mesh electrode, and the reference electrode was a BASi or CH Instruments Ag/AgCl reference electrode. All potentials reported in this manuscript were converted to NHE reference scale.

#### Cyclic voltammetry

Electrocatalyst films with geometric surface area of  $0.25~\text{cm}^2$  on ITO was used as the working electrode with Pt mesh as the auxiliary electrode and Ag/AgCl reference electrode. A two-compartment cell was used for cyclic voltammetry experiments filled with 0.1~m KOH (pH 13) solution. Cyclic voltammograms were collected at  $100~\text{mV}\,\text{s}^{-1}$ .

#### Tafel plots

Current-potential data were obtained by performing chronoamperometry in 0.1  $\,\mathrm{m}$  KOH electrolyte at a variety of applied potentials in a two-compartment cell. The geometric surface area of the catalyst was 0.25  $\,\mathrm{cm}^2$  prepared as mentioned above for **2-M** and **3-M**. Steady-state currents were measured at a variety of applied potentials while the solution was stirred, starting at 1.75 V and proceeding in 10  $\,\mathrm{m}$ V steps to 1.5 V vs. RHE. The current reached a steady state at a certain potential within 1–2  $\,\mathrm{min}$ . The measurements were made three times and averaged with the variation in steady-state current < 5  $\,\mathrm{\%}$ .

#### Rotating disk voltammetry

All activity, stability, and electrochemically-active surface area (ECSA) measurements on the glassy carbon (GC) disk electrodes were conducted with a Bio-Logic VMP3 multichannel potentiostat/ galvanostat with a built-in EIS analyzer. The working electrodes were 5 mm diameter disk electrodes, and catalysts were deposited as described above. The working electrodes were mounted in a Pine Instrument Company E6-series ChangeDisk rotating disk electrode assembly in an MSR rotator. The auxiliary electrodes were carbon rods (99.999%, Alfa Aesar), and the reference electrode was a commercial saturated calomel electrode (SCE; CH-Instruments) that was externally referenced to a solution of ferrocene monocarboxylic acid (Sigma-Aldrich) in a 0.2 м phosphate buffer at pH 7 (0.284 V vs SCE). [28] Data were recorded using the Bio-Logic EC-Lab and EC-Lab Express software packages. Electrochemical experiments were carried out according to a previously described protocol for the evaluation of heterogeneous electrocatalysts for the OER [9] to compare the OER performance of 2-Co and 2-Ni against selected electrodeposited electrocatalysts under identical conditions.

The electrochemically active surface area, ECSA, of each catalyst was determined by estimating the double-layer capacitance,  $C_{\rm DL}$ , of the system from cyclic voltammograms as previously described. Briefly, a non-Faradaic region was established for each system from CV. All current in this region is assumed to be due to double-layer charging, and, thus, the measured charging current,  $i_{c}$  is equal to the product of the scan rate,  $\nu$ , and the double-layer capacitance [Eq. (2)].  $^{[26-27]}$ 

$$i_{c} = \nu C_{DL}$$
 (2)

The ECSA is determined by dividing the estimated  $C_{\rm DL}$  of each system by the specific capacitance of the sample. For the purpose of this study, we use a specific capacitance of 0.040 mF cm<sup>-2</sup>, which is a typical value for a metal electrode in aqueous NaOH solution. [9] The ECSA values determined from these measurements are order of magnitude approximations for rough comparison of electroactive surface areas. [9i,k]

#### Oxygen evolution faradaic efficiency measurements

The experiment was performed in a custom-built two-compartment gas-tight electrochemical cell with a 14/20 port on each compartment and a Schlenk connection with a Teflon valve on the working compartment. The cell volume was 154 mL. A NeoFox oxygen-sensing system by Ocean Optics with FOXY fluorescence probe was used in O2 detection. The oxygen concentration was monitored throughout the measurement and was tabulated via measured values from a fluorescence detector. These values were calibrated using the standard concentration of oxygen in air as 20.9% partial pressure of O2 atmosphere. The cell was initially evacuated under vacuum. 54 mL of degassed 0.1 м KOH electrolyte solution was transferred by cannula into the cell under positive N<sub>2</sub> pressure, and the headspace used as a 0.0 % O<sub>2</sub> atmosphere. The calculated volume of the headspace was 96 mL. An Ag/AgCl reference electrode was placed in one compartment and the counter electrode was a Pt mesh positioned in a separate, fritted compart-

All catalysts used were prepared by subjecting the film through chronopotentiometry experiments for 5 h prior to oxygen evolution measurements. The ITO electrode with the catalyst film was clipped inside the electrochemical cell prior to evacuating the cell under vacuum, as mentioned above.





To ensure no leakage occurred, the partial pressure of  $O_2$  was measured for 2 h in the absence of an applied potential. Chronopotentiometry was run at a steady current of  $1\,\mathrm{mA\,cm^{-2}}$  for  $2\text{-}4\,\mathrm{h}$  with stirring of the solution. Upon termination of electrolysis, the  $O_2$  signal was recorded for an additional 2 h. At the conclusion of the experiment, the volume of the solution and the volume of the headspace in the working compartment were measured again (54 mL and 96 mL, respectively). The blue curve in Figure S4 (see the Supporting Information) was calculated by dividing the charge passed in the electrolysis by 4 F (theoretical yield) and the red curve was calculated by converting the measured partial pressure of  $O_2$  into  $\mu$ mols, correcting for the  $O_2$  in solution using Henry's Law (experimental yield).

#### Structural characterization

#### Powder X-Ray diffraction

Powder XRD patterns were obtained with a PANalytical X'Pert Pro rotating anode X-ray diffractometer (185 mm) using  $Cu_{K\alpha}$  radiation ( $\lambda = 1.5405$  Å). Data was collected at a scan rate of 1° per minute. A pattern was collected for an ITO-coated glass substrate and for the electrocatalysts prepared (see the Supporting Information, Figure S5). The ITO peaks were observed as the only signals arising from the XRD patterns of all electrocatalysts. Given that the final deposited catalyst sample is approximately 100 nm thick, the presence of peaks from the relatively thin ITO layer and the absence of any non-ITO-associated peaks indicate that the catalyst material is probably too thin or amorphous.

#### Scanning electron microscopy

Scanning-electron micrograph was obtained using a high-resolution analytical scanning electron microscope (ZEISS 1550VP) at an accelerating voltage of 10 kV with a working distance of 8 mm and an in-lens secondary electron detector.

#### X-ray absorption spectroscopy

X-ray absorption spectra of the electrode samples were collected at the Stanford Synchrotron Radiation Lightsource (SSRL) on beamline 7–3 at an electron energy of 3.0 GeV with an average current of 500 mA. The incoming X-ray was monochromatized by a Si(220) double-crystal monochromator. The intensity of the incident X-ray was monitored by an N<sub>2</sub>-filled ion chamber ( $I_0$ ) in front of the sample. Data were collected as fluorescence excitation spectra with a Ge 30 element detector (Canberra). The monochromator energy was calibrated by the pre-edge peak top of KMnO<sub>4</sub> standard at 6543.30 eV for Mn XAS, and the rising edge position of Ni foil at 8333.0 eV for Ni XAS. The standard was placed between two N<sub>2</sub>-filled ionization chambers ( $I_1$  and  $I_2$ ) after the sample. All data were collected *ex situ* at room temperature before or after electrochemistry.

Data reduction of the extended X-ray absorption fine structure (EXAFS) spectra was performed using SixPack (Dr. Samuel Webb, SSRL). Pre-edge and post-edge backgrounds were subtracted from the XAS spectra, and the results were normalized with respect to edge height. Background removal in *k*-space was achieved through a five-domain cubic spline. Curve fitting was performed with Artemis and IFEFFIT software using ab initio-calculated phases and amplitudes from the program FEFF 8.2.<sup>[29]</sup> These ab initio phases and amplitudes were used in the EXAFS equation:

$$\chi(k) = S_0^2 \sum_j \frac{N}{kR_j^2} f_{\text{eff}} j(\pi, k, R_j) e^{-2\sigma_j^2 k^2} e^{-2R_j/\lambda_j(k)} \sin(2kR_j + \phi_{ij}(k))$$
(3)

The neighboring atoms to the central atom(s) are divided into j shells, with all atoms with the same atomic number and distance from the central atom grouped into a single shell. Within each shell, the coordination number  $N_i$  denotes the number of neighboring atoms in shell j at a distance of  $R_i$  from the central atom. The  $f_{eff}j(\pi, k, R_i)$  term is the ab initio amplitude function for shell j, and the Debye-Waller term  $e^{-2\sigma_j^2k^2}$  accounts for damping due to static and thermal disorder in absorber-backscatterer distances. The mean free path term  $e^{-2R_j/\lambda_f(k)}$  reflects losses due to inelastic scattering, where  $\lambda_i(k)$  is the electron mean free path. The oscillations in the EXAFS spectrum are reflected in the sinusoidal term,  $\sin(2kR_i + \phi_{ij}(k))$  where  $\phi_{ij}(k)$  is the ab initio phase function for shell j.  $S_0^{\ 2}$  is an amplitude reduction factor due to shake-up/shakeoff processes at the central atom(s). The EXAFS equation was used to fit the experimental data using N, R, and the EXAFS Debye-Waller factor ( $\sigma^2$ ) as variable parameters.  $E_0$  was defined as 6561.3 eV and the S<sub>0</sub><sup>2</sup> value was fixed to 0.70 for the energy (eV) to wave vector (k,  $\mathring{A}^{-1}$ ) axis conversion for Mn XAS, and the  $E_0$  of 8340 eV and the  $S_0^2$  of 0.95 were used for Ni XAS.

#### **Elemental composition analyses**

#### X-ray photoelectron spectroscopy

XPS data were collected by using a Surface Science Instruments M-Probe ESCA controlled by Hawk Data Collection software (Service Physics, Bend OR; V7.04.04). The monochromatic X-ray source was the Al $_{K\alpha}$  line at 1486.6 eV, directed at 35° to the sample surface (55° off normal). Emitted photoelectrons were collected at an angle of 35° with respect to the sample surface (55° off normal) by a hemispherical analyzer. The angle between the electron collection lens and X-ray source is 71°. Low-resolution survey spectra were acquired between binding energies of 1–1100 eV. Higher resolution scans, with a resolution of about 0.8 eV, were collected on individual XPS lines of interest. The sample chamber was maintained at  $<\!2\times10^{-9}$  Torr. Spectra were analyzed by using the Hawk Data Analysis software (V7.04.04) and the CasaXPS Version 2.3.15 software package.

### Energy dispersive X-ray spectroscopy (EDS) and elemental mapping

An Oxford X-Max SDD energy-dispersive X-ray spectrometer (EDS) equipped in the SEM instrument was used at a working distance of 12 mm using an accelerating voltage of 20 kV.

#### Inductively coupled-mass spectrometry (ICP-MS)

Inductively coupled plasma mass spectrometry (ICP-MS) data were collected using a Hewlett–Packard 4500 ICP-MS System with a Babbington nebulizer and a Scott-type spray chamber maintained at 5  $^{\circ}$ C. The plasma was operated at 1250 W. All samples were diluted to concentrations of 10–20 ppb and analyzed against a standard curve of known concentrations of specific metals.



# CHEMISTRY A European Journal Full Paper

#### **Acknowledgements**

This work was supported by Caltech, the NSF CAREER grant CHE-1151918 and the NIH grant R01 GM102687A (T.A.). T.A. is a Sloan, Cottrell, and Dreyfus fellow. Rotating-disk voltammetry and 2 h stability measurements are based on work performed by the Joint Center for Artificial Photosynthesis, a DOE Energy Innovation Hub, supported through the Office of Science of the U.S. Department of Energy under award no. DE-SC0004993. Portions of this research were carried out at the SSRL, operated by Stanford University for the U.S. DOE Office of Science, and supported by the DOE and NIH. X-ray spectroscopy studies were supported by the NIH (R.T.) and by the Director of the OBES, Division of Chemical Sciences, Geosciences, and Biosciences, DOE (J.Y.). We thank James D. Blakemore for helpful discussions, Nathan Dalleska for assistance in ICP-MS data acquisition, and Tim Davenport for assistance in TGA studies. We thank Dr. Jordi Cabana and Dr. Ulrike Boesenberg for providing the NiO reference spectrum. Research was in part carried out at the Molecular Materials Research Center of the Beckman Institute of the California Institute of Technology. This project benefited from the use of instrumentation made available by the Caltech Environmental Analysis Center.

**Keywords:** cubanes • electrocatalysis • manganese • metal oxides • oxygen evolution reaction

- [1] a) T. R. Cook, D. K. Dogutan, S. Y. Reece, Y. Surendranath, T. S. Teets, D. G. Nocera, Chem. Rev. 2010, 110, 6474–6502; b) M. G. Walter, E. L. Warren, J. R. McKone, S. W. Boettcher, Q. X. Mi, E. A. Santori, N. S. Lewis, Chem. Rev. 2010, 110, 6446–6473; c) S. Trasatti in Interfacial Electrochemistry: Theory, Practice, Applications (Ed.: A. Wieckowski), Marcel Dekker, New York, 1999.
- [2] a) M. W. Kanan, D. G. Nocera, Science 2008, 321, 1072 1075; b) Y. Gorlin, T. F. Jaramillo, J. Am. Chem. Soc. 2010, 132, 13612-13614; c) M. Dinca, Y. Surendranath, D. G. Nocera, Proc. Natl. Acad. Sci. USA 2010, 107, 10337 -10341; d) I. Zaharieva, P. Chernev, M. Risch, K. Klingan, M. Kohlhoff, A. Fischer, H. Dau, *Energy Environ. Sci.* 2012, 5, 7081 – 7089; e) N. D. Schley, J. D. Blakemore, N. K. Subbaiyan, C. D. Incarvito, F. D'Souza, R. H. Crabtree, G. W. Brudvig, J. Am. Chem. Soc. 2011, 133, 10473 - 10481; f) J. Suntivich, K. J. May, H. A. Gasteiger, J. B. Goodenough, Y. Shao-Horn, Science 2011, 334, 1383-1385; g) R. Subbaraman, D. Tripkovic, K. C. Chang, D. Strmcnik, A. P. Paulikas, P. Hirunsit, M. Chan, J. Greeley, V. Stamenkovic, N. M. Markovic, Nat. Mater. 2012, 11, 550-557; h) F. Jiao, H. Frei, Energy Environ. Sci. 2010, 3, 1018-1027; i) J. H. Yang, K. Walczak, E. Anzenberg, F. M. Toma, G. B. Yuan, J. Beeman, A. Schwartzberg, Y. J. Lin, M. Hettick, A. Javey, J. W. Ager, J. Yano, H. Frei, I. D. Sharp, J. Am. Chem. Soc. 2014, 136, 6191-6194; j) E. M. W. Rumberger, H. S. Ahn, A. T. Bell, T. D. Tilley, Dalton Trans. 2013, 42, 12238-12247; k) I. Zaharieva, M. M. Najafpour, M. Wiechen, M. Haumann, P. Kurz, H. Dau, Energy Environ. Sci. 2011, 4, 2400 - 2408.
- [3] a) J. Rossmeisl, A. Logadottir, J. K. Norskov, Chem. Phys. 2005, 319, 178 –
   184; b) B. E. Conway, B. V. Tilak in Advances in Catalysis, Vol. 38 (Eds.: D. D. Eley, H. Pines, P. B. Weisz), Academic Press, New York, 1992.
- [4] a) J. O. Bockris, T. Otagawa, J. Phys. Chem. 1983, 87, 2960 2971; b) J. O. Bockris, T. Otagawa, J. Electrochem. Soc. 1984, 131, 290 302.
- [5] P. Rasiyah, A. C. C. Tseung, J. Electrochem. Soc. 1984, 131, 803 808.
- [6] S. Trasatti, J. Electroanal. Chem. 1980, 111, 125-131.
- [7] a) Y. Matsumoto, E. Sato, Mater. Chem. Phys. 1986, 14, 397–426; b) J. P. Hoare in Encyclopedia of Electrochemistry of the Elements, Vol. 2 (Ed.: A. J. Bard), Marcel Dekker, New York, 1982.

www.chemeurj.org

[8] S. Trasatti, *Electrochim. Acta* **1984**, *29*, 1503 – 1512.

- [9] a) D. A. Corrigan, J. Electrochem. Soc. 1987, 134, 377-384; b) D. A. Corrigan, R. M. Bendert, J. Electrochem. Soc. 1989, 136, 723-728; c) M. D. Merrill, R. C. Dougherty, J. Phys. Chem. C 2008, 112, 3655-3666; d) L. Trotochaud, S. L. Young, J. K. Ranney, S. W. Boettcher, J. Am. Chem. Soc. 2014, 136, 6744-6753; e) J. Landon, E. Demeter, N. Inoglu, C. Keturakis, I. E. Wachs, R. Vasic, A. I. Frenkel, J. R. Kitchin, ACS Catal. 2012, 2, 1793-1801; f) M. Gong, Y. G. Li, H. L. Wang, Y. Y. Liang, J. Z. Wu, J. G. Zhou, J. Wang, T. Regier, F. Wei, H. J. Dai, J. Am. Chem. Soc. 2013, 135, 8452-8455; g) M. W. Louie, A. T. Bell, J. Am. Chem. Soc. 2013, 135, 12329-12337; h) L. Trotochaud, J. K. Ranney, K. N. Williams, S. W. Boettcher, J. Am. Chem. Soc. 2012, 134, 17253-17261; i) C. C. L. McCrory, S. H. Jung, J. C. Peters, T. F. Jaramillo, J. Am. Chem. Soc. 2013, 135, 16977 - 16987; j) A. M. Smith, L. Trotochaud, M. S. Burke, S. W. Boettcher, Chem. Commun. 2015, 51, 5261-5263; k) C. C. L. McCrory, S. Jung, I. M. Ferrer, S. M. Chatman, J. C. Peters, T. F. Jaramillo, J. Am. Chem. Soc. 2015, 137, 4347 - 4357.
- [10] a) S. M. Jasem, A. C. C. Tseung, J. Electrochem. Soc. 1979, 126, 1353–1360; b) J. C. K. Ho, D. L. Piron, J. Appl. Electrochem. 1996, 26, 515–521.
- [11] a) A. K. M. Fazle Kibria, S. A. Tarafdar, Int. J. Hydrogen Energy 2002, 27, 879–884; b) X. H. Li, F. C. Walsh, D. Pletcher, Phys. Chem. Chem. Phys. 2011, 13, 1162–1167.
- [12] M. S. Burke, M. G. Kast, L. Trotochaud, A. M. Smith, S. W. Boettcher, J. Am. Chem. Soc. 2015, 137, 3638 3648.
- [13] R. N. Singh, Madhu, R. Awasthi, A. S. K. Sinha, *Electrochim. Acta* 2009, 54, 3020 – 3025.
- [14] R. N. Singh, Madhu, R. Awasthi, S. K. Tiwari, Int. J. Hydrogen Energy 2009, 34, 4693 – 4700.
- [15] R. N. Singh, J. P. Pandey, N. K. Singh, B. Lal, P. Chartier, J. F. Koenig, *Electrochim. Acta* 2000, 45, 1911 1919.
- [16] a) M. Wiechen, I. Zaharieva, H. Dau, P. Kurz, Chem. Sci. 2012, 3, 2330–2339; b) J. Kim, X. Yin, K. C. Tsao, S. H. Fang, H. Yang, J. Am. Chem. Soc. 2014, 136, 14646–14649.
- [17] R. N. Singh, N. K. Singh, J. P. Singh, Electrochim. Acta 2002, 47, 3873–3879.
- [18] a) J. Y. C. Chen, J. T. Miller, J. B. Gerken, S. S. Stahl, Energy Environ. Sci. 2014, 7, 1382–1386; b) J. B. Gerken, S. E. Shaner, R. C. Masse, N. J. Porubsky, S. S. Stahl, Energy Environ. Sci. 2014, 7, 2376–2382; c) J. B. Gerken, J. Y. C. Chen, R. C. Masse, A. B. Powell, S. S. Stahl, Angew. Chem. Int. Ed. 2012, 51, 6676–6680; Angew. Chem. 2012, 124, 6780–6784; d) J. A. Haber, Y. Cai, S. H. Jung, C. X. Xiang, S. Mitrovic, J. Jin, A. T. Bell, J. M. Gregoire, Energy Environ. Sci. 2014, 7, 682–688.
- [19] a) J. A. Haber, C. X. Xiang, D. Guevarra, S. H. Jung, J. Jin, J. M. Gregoire, Chemelectrochem. 2014, 1, 524–528; b) S. Cattarin, I. Frateur, P. Guerriero, M. Musiani, Electrochim. Acta 2000, 45, 2279–2288.
- [20] a) R. D. L. Smith, M. S. Prevot, R. D. Fagan, Z. P. Zhang, P. A. Sedach, M. K. J. Siu, S. Trudel, C. P. Berlinguette, *Science* 2013, 340, 60–63;
  b) R. D. L. Smith, M. S. Prevot, R. D. Fagan, S. Trudel, C. P. Berlinguette, *J. Am. Chem. Soc.* 2013, 135, 11580–11596; c) C. J. Zhang, S. Trudel, C. P. Berlinguette, *Eur. J. Inorg. Chem.* 2014, 660–664.
- [21] a) Y. Gorlin, C. J. Chung, J. D. Benck, D. Nordlund, L. Seitz, T. C. Weng, D. Sokaras, B. M. Clemens, T. F. Jaramillo, J. Am. Chem. Soc. 2014, 136, 4920–4926; b) Y. Gorlin, B. Lassalle-Kaiser, J. D. Benck, S. Gul, S. M. Webb, V. K. Yachandra, J. Yano, T. F. Jaramillo, J. Am. Chem. Soc. 2013, 135, 8525–8534.
- [22] a) M. D. Karkas, O. Verho, E. V. Johnston, B. Akermark, Chem. Rev. 2014. 114, 11863 - 12001; b) A. M. Ullman, Y. Liu, M. Huynh, D. K. Bediako, H. S. Wang, B. L. Anderson, D. C. Powers, J. J. Breen, H. D. Abruna, D. G. Nocera, J. Am. Chem. Soc. 2014, 136, 17681 - 17688; c) M. M. Najafpour, A. N. Moghaddam, H. Dau, I. Zaharieva, J. Am. Chem. Soc. 2014, 136, 7245 - 7248; d) M. Wiechen, H. M. Berends, P. Kurz, Dalton Trans. 2012, 41, 21-31; e) R. K. Hocking, R. Brimblecombe, L. Y. Chang, A. Singh, M. H. Cheah, C. Glover, W. H. Casey, L. Spiccia, Nat. Chem. 2011, 3, 461 -466; f) R. Brimblecombe, G. F. Swiegers, G. C. Dismukes, L. Spiccia, Angew. Chem. Int. Ed. 2008, 47, 7335-7338; Angew. Chem. 2008, 120, 7445-7448; g) J. J. Stracke, R. G. Finke, J. Am. Chem. Soc. 2011, 133, 14872 - 14875; h) M. Yagi, K. Narita, J. Am. Chem. Soc. 2004, 126, 8084 -8085; i) Y. H. Lai, T. C. King, D. S. Wright, E. Reisner, Chem. Eur. J. 2013, 19, 12943 – 12947; j) Y. H. Lai, C. Y. Lin, Y. K. Lv, T. C. King, A. Steiner, N. M. Muresan, L. H. Gan, D. S. Wright, E. Reisner, Chem. Commun. 2013, 49, 4331-4333.





- [23] a) J. S. Kanady, E. Y. Tsui, M. W. Day, T. Agapie, Science 2011, 333, 733 736; b) E. Y. Tsui, T. Agapie, Proc. Natl. Acad. Sci. USA 2013, 110, 10084 10088
- [24] a) D. K. Bediako, B. Lassalle-Kaiser, Y. Surendranath, J. Yano, V. K. Yachandra, D. G. Nocera, J. Am. Chem. Soc. 2012, 134, 6801–6809; b) M. W. Kanan, J. Yano, Y. Surendranath, M. Dinca, V. K. Yachandra, D. G. Nocera, J. Am. Chem. Soc. 2010, 132, 13692–13701.
- [25] a) Y. Umena, K. Kawakami, J. R. Shen, N. Kamiya, *Nature* **2011**, *473*, 55 U65; b) K. N. Ferreira, T. M. Iverson, K. Maghlaoui, J. Barber, S. Iwata, *Science* **2004**, *303*, 1831 1838.
- [26] J. D. Benck, Z. B. Chen, L. Y. Kuritzky, A. J. Forman, T. F. Jaramillo, ACS Catal. 2012, 2, 1916–1923.
- [27] a) S. Trasatti, O. A. Petrii, Pure Appl. Chem. 1991, 63, 711-734; b) J. O.
   Bockris, S. Srinivas, J. Electroanal. Chem. 1966, 11, 350; c) R. Boggio, A.
   Carugati, S. Trasatti, J. Appl. Electrochem. 1987, 17, 828-840.
- [28] E. Liaudet, F. Battaglini, E. J. Calvo, J. Electroanal. Chem. 1990, 293, 55–68
- [29] a) M. Newville, J. Synchrotron Radiat. 2001, 8, 322–324; b) J. J. Rehr, R. C. Albers, Rev. Mod. Phys. 2000, 72, 621–654.

Received: March 20, 2015 Published online on August 4, 2015

www.chemeurj.org